Journal of MATERIALS RESEARCH

Article
DOI:10.1557/s43578-021-00229-y

MULTIFUNCTIONAL HALIDE PEROVSKITES

FOCUS ISSUE

Probing structure–property relationship in chemical vapor deposited hybrid perovskites by pressure and temperature

Randy Burns[1], Siphelo Ngqoloda[2], Christopher J. Arendse[2], Barbara Lavina[3,4], Ashutosh Dahal[1], Deepak K. Singh[1], Suchismita Guha[1,a)]

[1] Department of Physics and Astronomy, University of Missouri, Columbia, MO 65211, USA
[2] Department of Physics and Astronomy, University of the Western Cape, Private Bag X17, Bellville 7535, South Africa
[3] University of Chicago, GeoSoilEnviro Center for Advanced Radiation Sources, Chicago, IL 60637, USA
[4] X-ray Science Division, Advanced Photon Source, Argonne National Laboratory, Argonne, IL 60349, USA
[a)] Address all correspondence to this author. e-mail: guhas@missouri.edu

Received: 29 January 2021; accepted: 28 April 2021

Chemical vapor deposition (CVD), a low-cost and a scalable deposition technique, allows the growth of methylammonium lead iodide ($MAPbI_3$) films without the use of solvents, substantially increasing air stability while also inducing the stable cubic phase at room temperature and at pressures as low as 0.25 GPa. $MAPbI_3$ thin films were grown by a facile two-step low-pressure vapor deposition process in a single reactor. This method results in films, which are usually in the tetragonal phase (space group: *I4/mcm*) and occasionally in the cubic phase under ambient conditions. High-pressure synchrotron-based X-ray diffraction studies from CVD-grown $MAPbI_3$ crystallites show that the sample remains in the cubic phase (space group: $Im\bar{3}$) between 0.25 and 3.0 GPa. Temperature-dependent transport measurements show sharp anomalies, correlating with the structural changes. The transport measurements from the CVD-grown cubic $MAPI_3$ film is further compared with a film in the tetragonal phase.

Introduction

No other semiconductor has shown such a rapid increase in solar cell power conversion efficiencies (PCE) over a period of 10 years as the organic–inorganic hybrid perovskites (OIHP). In addition to applications in solar cells, OIHPs show great promise in other opto/electronic devices such as displays, photodetectors, and sensors [1]. Among OIHPs, which share a general formula of ABX_3, the structural properties of methylammonium (MA) OIHPs: $MAPbX_3$ (MA^+=$CH_3NH_3^+$ and X^- = Cl^-, Br^-, or I^-) have been known for over 40 years [2]. The structural properties of OIHPs change as a function of temperature and pressure, and these attributes are strongly related to the halogen ion in $MAPbX_3$. The PbX_6 octahedra form the framework by corner sharing with MA^+, which is coordinated to the halogen ion. Under ambient conditions, $MAPbBr_3$ usually has a cubic symmetry ($Pm\bar{3}m$) whereas $MAPbI_3$ is mainly in the tetragonal phase (*I4/mcm*). The effective radii of the ions dictate the tolerance factor, $t = \frac{r_A + r_X}{\sqrt{2}(r_B + r_X)}$, where r_A, r_B, and r_X are the radii of the organic cation, inorganic cation, and the halide anion, and the octahedra factor, $o_c = \frac{r_B}{r_X}$. The OIHPs usually possess a cubic symmetry when $0.813 \leq t \leq 1.107$ and $0.442 \leq o_c \leq 0.895$, otherwise, it is in the tetragonal or orthorhombic structure [3]. Along with the radii of the ions, the dynamical coupling of the MA^+ with X^- via hydrogen bonds may result in deviation from the cubic phase by tilting of the octahedra [4, 5]. What is less known in the literature is how the same perovskite crystal may adopt a slightly different structure depending on the growth method. In this work, we focus on $MAPbI_3$ films grown by chemical vapor deposition. The structural and transport properties are investigated as a function of pressure and temperature, respectively.

Much of the development of OIHP films for optoelectronics involves solution processing, where the precursors are dissolved in appropriate solvents. Spin-coating OIHP films comes with its own challenges of non-uniform coverage and solvent incompatibility in multiple layers, which may further lead to macroscopic

defect sites that act as pathways for moisture ingression and/or device instability. Among spin-coated films, the use of ionic additives has been beneficial for the performance of solar cells with degradation by only 5% under continuous (simulated) sunlight for over 75 days [6]. Air stability is still an issue and most solar cells are encapsulated. There is also a push towards spray-coated perovskite films, which when utilized in solar cells have demonstrated PCE > 19% [7]. Vapor deposition methods, including both physical vapor deposition (PVD) and chemical vapor deposition (CVD), have proven to be controllable and repeatable methods for depositing perovskite films. These methods are either single step with simultaneous deposition of the organic cation and the metal halide, or involve a two-step sequential deposition [8–12]. In another work, a three-step vapor deposition using PbSe as the first precursor layer yielded $MAPbI_3$ in the cubic phase under ambient conditions [13]. Reports of speeding up the vapor deposition process of perovskite films may further prove to be a cost-effective scalable manufacturing process [14].

Our prior work demonstrated a two-step method of depositing $MAPbI_3$ films in a CVD reactor. First, a PbI_2 film is vapor deposited and then, using the same reactor, the film is converted to a uniform, polycrystalline $MAPbI_3$ perovskite thin film by exposure to MAI vapors. This method produces high-quality films on different substrates such as glass, indium tin oxide-coated glass, and Si. In contrast to spin-coating methods, CVD introduces precursor material to substrates in a more uniform manner which can significantly impact sample morphology. Consequently, the increased atmospheric stability of our CVD-grown films manifests from a combination of superior surface coverage of the perovskite layer, vertically orientated grain columns, and lack of moisture-trapping pinholes [15]. Air stability of these films was observed for several days, and the best PCE of solar cells fabricated from CVD-grown $MAPbI_3$ film was just under 12%.

OIHPs provide a test bed for tuning their structural and optoelectronic properties via pressure and temperature. In contrast to chemical pressure, hydrostatic pressure can continuously tune the structural properties and, therefore, the electronic states, without changing the chemical make-up. Since several phase transitions under pressure and temperature in OIHPs are close to ambient conditions, it becomes pertinent to map the phase-structure properties with precision. $MAPbI_3$ crystals and films cast from a solution process are seen to stabilize in the tetragonal phase (SG (space group): $I4/mcm$) at room temperature (ambient conditions), in the orthorhombic phase (SG: $Pnma$) below 160 K, and in the cubic phase (SG: $Pm\bar{3}m$) above 327 K [16, 17]. Under pressure (at room temperature), single-crystal $MAPbI_3$ is seen to undergo a tetragonal to cubic phase II transition (SG: $Im\bar{3}$) at 0.35 GPa, which remains stable until ~ 2.5 GPa, where the crystal is seen to undergo a gradual amorphization [18]. In the work by Jaffe et al., the ambient-pressure $MAPbI_3$ (single crystal) was observed to be in the orthorhombic space group (SG: $Fmmm$) with a phase transition to the cubic phase II at ~ 0.4 GPa [19].

We present structural and optical properties of CVD-grown polycrystalline $MAPbI_3$ under ambient conditions, followed by synchrotron-based high-pressure X-ray diffraction (XRD). Between 0.25 and 3.0 GPa, the sample is seen to be in the cubic phase II. For a film of $MAPbI_3$ grown on SiO_2/Si, the ambient structure was seen to be in the cubic phase (SG: $Im\bar{3}$). Four-probe temperature-dependent resistance measurements show sharp changes at 288 K, 162 K, and 56 K, which correlate with temperature-dependent lab-based XRD data. This study highlights the benefits of alternate growth methods for $MAPbI_3$ films. Figure 1 shows a schematic of the setup and optical images of the films. The CVD technique not only produces enhanced air-stable films but also, depending on the substrate and growth conditions, may result in the stable ambient cubic phase where ionic transport is further mitigated. The cubic phase is desirable for long-term stability of optoelectronic devices.

Results and discussion

Structural and optical properties of $MAPbI_3$ on glass

The films of $MAPbI_3$ grown on glass were characterized using XRD and optical absorption. Figure 2a shows a representative synchrotron-based powder ambient XRD data with a Le Bail fit. These measurements were carried out from different regions of the film (by scraping off the polycrystalline grains). They all show an identical XRD pattern with the tetragonal symmetry (SG: $I4/mcm$). The calculated lattice parameters are found to be $a = b = 8.881$ (1) Å, $c = 12.633$ (5) Å, which agree with other reports [16]. No diffraction peaks of PbI_2 phase are present, highlighting that the film is fully converted into the perovskite structure.

Figure 2b shows the absorption spectrum from a $MAPbI_3$ film. The absorption spectrum near the band edge was simulated using the Elliott formalism [20]. Using the analysis by Haug and Koch [21], the band-edge absorption (α (ω)) can be expressed as follows:

$$\alpha(\omega) = \alpha_0^{3D}\frac{\hbar\omega}{E_0}\left[\sum_{n=1}^{\infty}\frac{4\pi}{n^3}\delta\left(\Delta+\frac{1}{n^2}\right)+\Theta(\Delta)\frac{\pi e^{-\pi/\sqrt{\Delta}}}{\sin h\left(\pi/\sqrt{\Delta}\right)}\right], \quad (1)$$

where $\Delta = \frac{(\hbar\omega - E_g)}{E_0}$, E_g is the band-gap energy, E_0 is the exciton binding energy, and n is the principal quantum number. The first term in the above expression refers to the excitonic state and the second term represents the continuum. A Gaussian line broadening function was used for fitting the experimental absorption spectrum. We obtain the excitonic binding energy as 70 meV

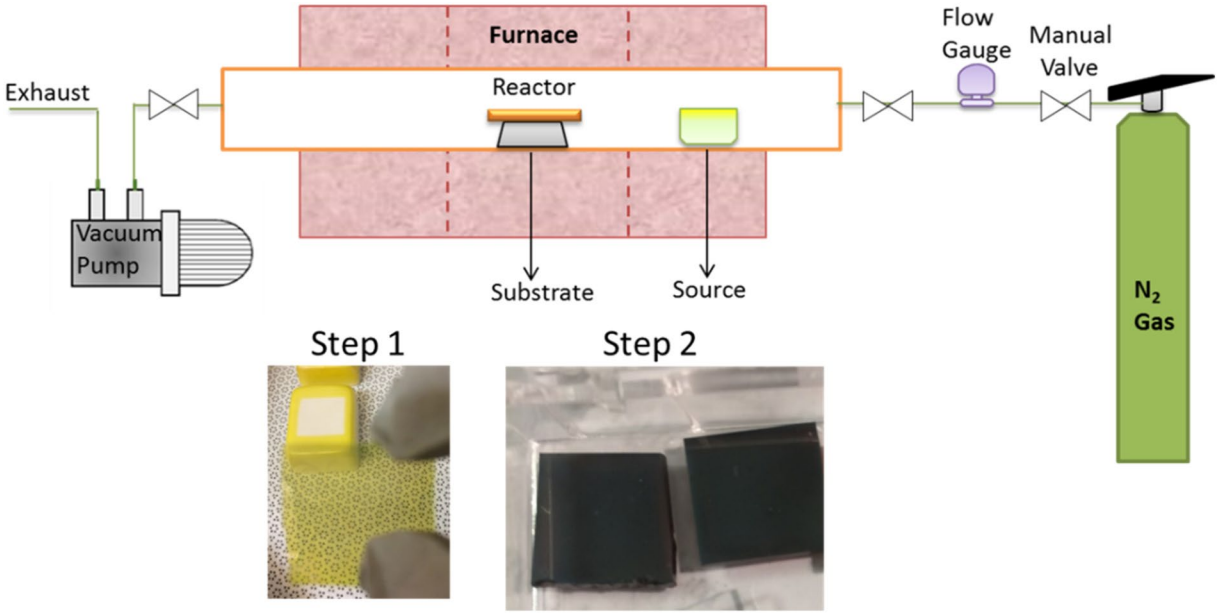

Figure 1: Schematic of the CVD system. Optical images of PbI_2 (step 1) and the fully converted $MAPbI_3$ (step 2) films are shown below.

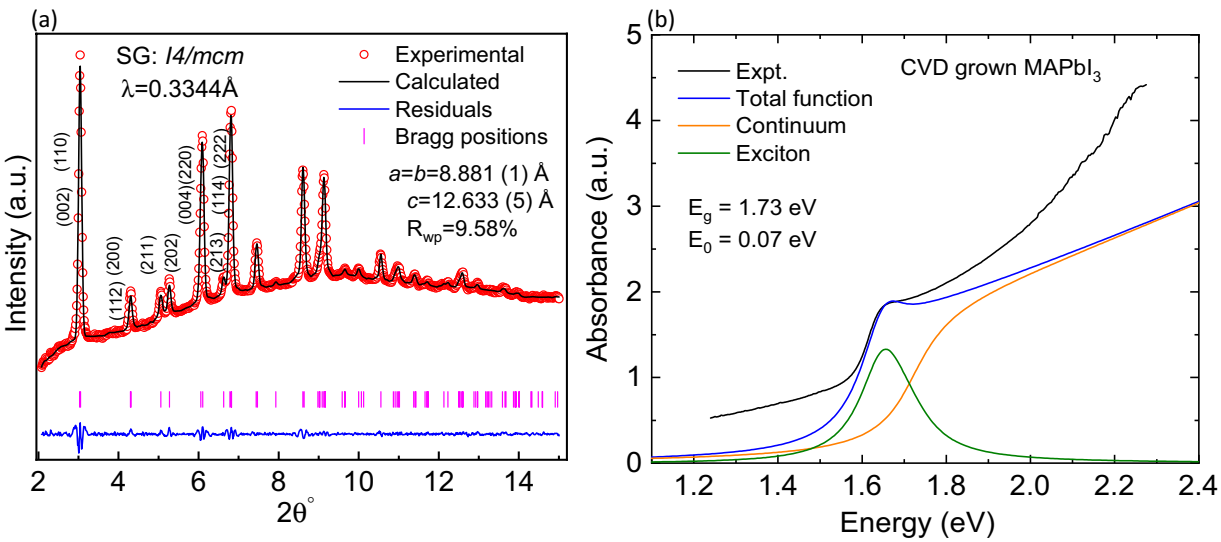

Figure 2: (a) A Le Bail fit of the XRD data from tetragonal (*SG I4/mcm*) $MAPbI_3$ (under ambient condition) with indexed planes and lattice constants indicated. The experimental and calculated XRD pattern are shown as red circles and black line, respectively. The small vertical lines and the blue pattern are the Bragg positions and difference spectra (residuals), respectively. (b) Simulated and experimental optical absorption from a $MAPbI_3$ film. The black curve is the experimental data. The blue curve represents the total function (Eq. (1)), which is further shown as the excitonic component (green) and the continuum (orange).

from the fit. The absorption spectrum remains unchanged for almost 3 weeks even when the samples are left under uncontrolled ambient conditions (temperature and humidity). Details of such studies were provided in Ref. [15].

The application of CVD-grown $MAPbI_3$ films in solar cells and their air stability have already been demonstrated. The solar cell maintains 85% of its performance up to 2 weeks in open air with a relative humidity up to 80% [15]. Here, we delve into other structural aspects, namely, phase transitions as a function of high pressure and temperature, and whether these transitions differ from crystals/polycrystals grown from solution processes.

High-pressure structural studies of CVD-grown $MAPbI_3$

Synchrotron high-pressure measurements were conducted on a powder sample of a CVD-grown $MAPbI_3$ thin film in order to detect any anomalous structural behavior in contrast to reported transitions from single crystal or spin-coated fabrication

methods using solution processing. Figure 3a shows stacked powder X-ray diffraction (PXRD) plots taken from 0.5 to 3.5 GPa and then down to 0.25 GPa upon pressure release. A uniform shift of the Bragg peaks toward higher angles is seen, as expected for the compression of a cubic phase, whereas intensity ratios remain roughly the same from 0.25 GPa until 2.3 GPa. These observations suggest that all spectra in the aforementioned range share the same phase. Beyond 2.3 GPa, we observe a progressive loss of the Bragg peak intensities, signaling gradual amorphization. Figure 3b demonstrates a fitting of the 0.25 GPa and 2.0 GPa spectra with a Le Bail refinement. Both spectra belong to the SG: $Im\bar{3}$ (cubic phase II), which is a doubling of the cubic phase I (SG: $Pm\bar{3}m$) due to the tilting of PbI_6 octahedral cage. Furthermore, the (211) peak at 5.1° that is unique to the tetragonal phase is completely absent in Fig. 3a as compared to Fig. 2a. The peak splitting in the tetragonal phase of the (222) peak at 6.9° is also absent from the spectra in Fig. 3a. These characteristics provide strong evidence for the cubic phase at 0.25 GPa. The observation of the SG: $Im\bar{3}$ for $MAPbI_3$ has not been realized at low pressures of 0.25 GPa. Other works have reported this phase transition at pressures upwards of 0.35 GPa [18, 19]. We attribute the presence of the $Im\bar{3}$ phase at lower pressures than previously reported to the specific CVD growth method used that presents a higher affinity towards the manifestation of the cubic phase. Interestingly, Lee et al predicted the transition to the $Im\bar{3}$ phase at 0.23 GPa using first-principles density functional theory calculations with lattice constants of $a = 12.370$ Å, $b = 12.403$ Å, and $c = 12.388$ Å [22]. At 0.25 GPa, we obtain the same $Im\bar{3}$ phase with lattice constants $a = b = c = 12.38$ (1) Å.

As expected, the volume of the unit cell systematically decreases as a function of pressure between 0.25 and 3.5 GPa shown in Fig. 4. At each pressure point, a Le Bail fit yielded the lattice parameters. The ambient-pressure data in the *I4/mcm* phase have Z = 4 whereas all other pressure points were in the $Im\bar{3}$ phase with $Z = 8$. The change in the slope beyond 2.5 GPa indicates an onset of amorphization. The inset shows an image of the DAC at 0.5 GPa with the sample and a piece of ruby.

Temperature-dependent transport measurements

Although several studies of $MAPbI_3$ have shed light on structural phase transformations as a function of temperature [16, 23], there are very few transport measurements as a function of temperature. This is predominantly due to the dominance of ionic conductivity over electronic conductivity under dark conditions [24, 25], necessitating sample illumination during conductivity measurements [26]. Other factors include growth methods. As an example, electrical properties of $MASnI_3$ are known to be sensitive to the preparation method; both metallic and semiconducting type behavior in resistivity as a function of temperature have been detected [27]. The anomalies in resistivity track with the structural transitions with temperature. More

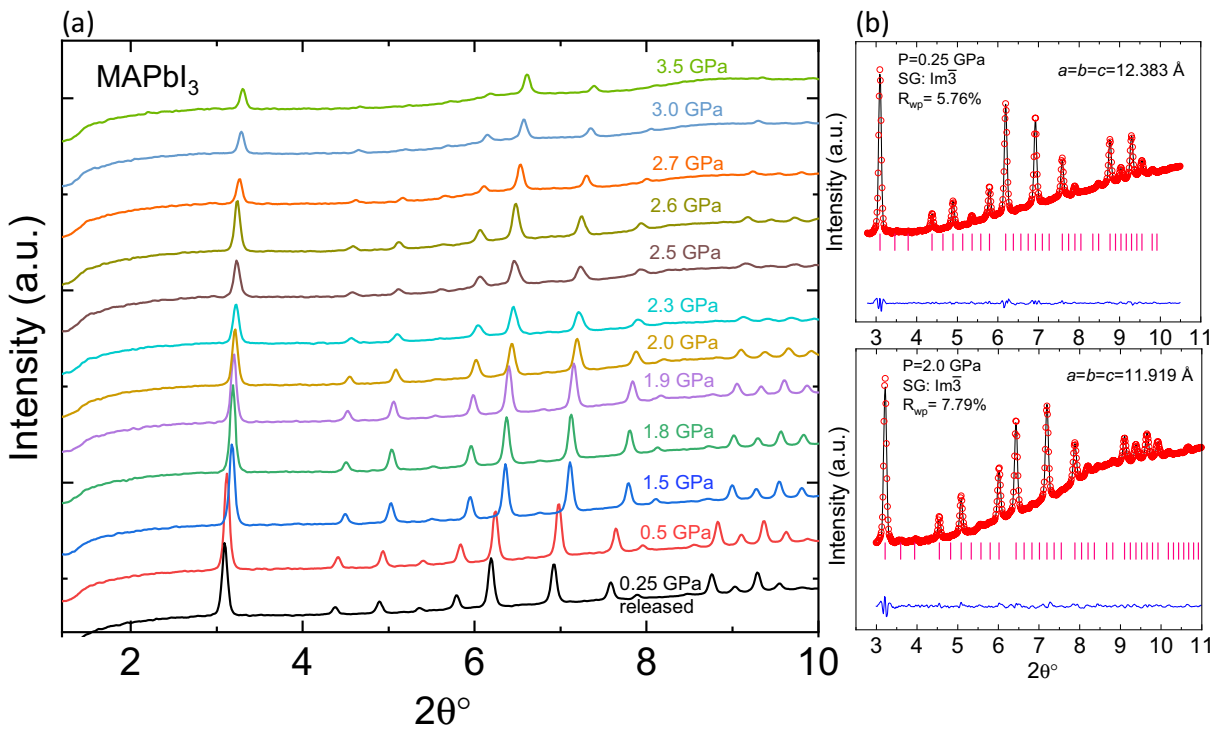

Figure 3: High-pressure synchrotron XRD pattern of $MAPbI_3$. (a) The XRD pattern at selected values of pressure. (b) Two XRD patterns of $MAPbI_3$ fit using the Le Bail refinement method at 0.25 GPa and 2.0 GPa demonstrating the same $Im\bar{3}$ phase.

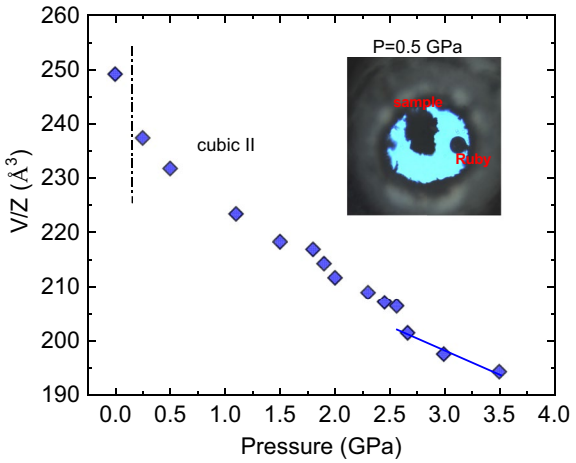

Figure 4: Molecular volume (V/Z) of $MAPbI_3$ as a function of pressure. The vertical dotted line indicates the two different crystal phases: the tetragonal phase at ambient pressure and the cubic II phase upwards of 0.25 GPa. The inset shows an optical image of the DAC at 0.5 GPa.

recently, a semiconductor–metal transition in $MAPbI_3$ thin films has been observed below the tetragonal-orthorhombic phase transition temperature, and the features in the resistivity were strongly dependent on the illumination and electric fields [28].

The above studies motivated us to investigate the temperature-dependent resistivity from CVD-grown $MAPbI_3$ films grown on different substrates. For an individual film grown on SiO_2, the ambient structure was found to be in the cubic phase. The exact mechanism that leads to the realization of the cubic phase is under investigation; however, a study exists that confirms that altering the rate of deposition of lead iodide in a vacuum deposition system can facilitate the room-temperature cubic phase and significantly improve solar cell performance [29]. As a result, one can conclude that the reaction rate of the lead iodide with the methylammonium iodide can determine the resultant phase. For our system, the possibility exists that the differences in thermal conductivity between glass and SiO_2 alter the substrate temperature and, consequently, the reaction rate between lead iodide and methylammonium iodide to manifest the room-temperature cubic phase. The room-temperature cubic phase shows a much lower resistance compared with films that are in the tetragonal phase at room temperature. Figure 5a shows the resistance versus temperature (as ratio of the resistance at a particular temperature to the resistance at 300 K) measured using a 4-probe method from a CVD-grown $MAPbI_3$ film on SiO_2 substrate in the range 5–300 K. These measurements were performed without any illumination and were completely reversible. The inset plots the same data in terms of the absolute resistance. A CVD-grown $MAPbI_3$ film on glass, in the tetragonal phase at room temperature, shows a different dependence of resistance with temperature, as shown in Fig. 5b. This film exhibited orders of magnitude higher resistance compared with the film grown on SiO_2 (see inset). A trend of decreasing resistance in the tetragonal phase, as in Fig. 5b, has been seen in other recent works [28].

In order to understand the trend in the resistance vs temperature in Fig. 5a, we have conducted laboratory-based temperature-dependent PXRD from the same sample. Although the low intensity of the PXRD data precluded a detailed Rietveld analysis, we were able to extract the structural information using a Le Bail fit. The sharp changes in the resistance correlate with the structural aspects quite well, as discussed below.

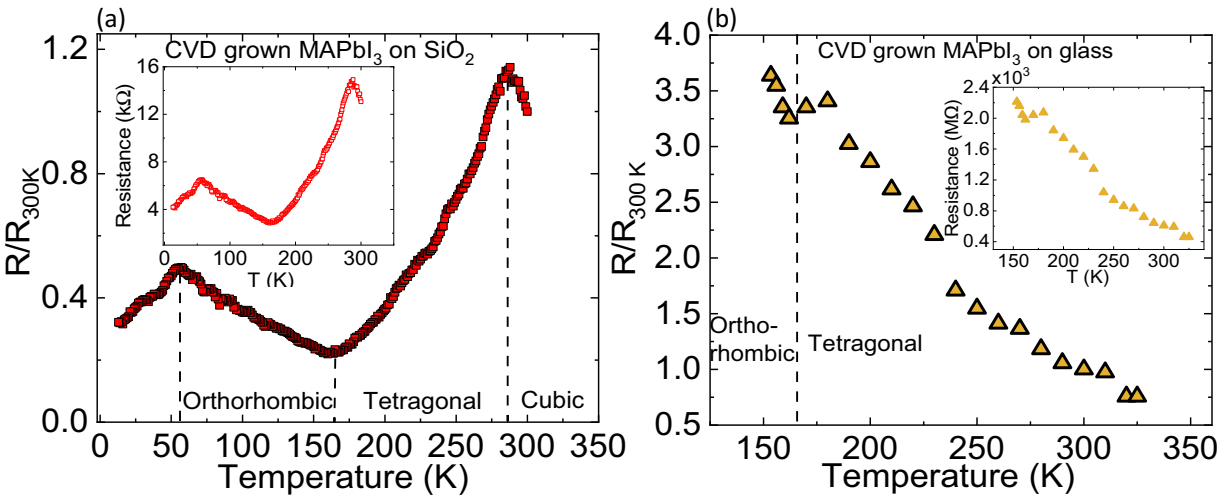

Figure 5: (a) Ratio of the resistance at temperature T to the resistance at 300 K as a function of temperature from a CVD-grown $MAPbI_3$ film on SiO_2. (b) Ratio of the resistance at temperature T to the resistance at 300 K as a function of temperature from a $MAPbI_3$ film grown on glass. The insets in (a) and (b) plot the absolute value of the resistance.

The PXRD data of the same $MAPbI_3$ sample (as in Fig. 5a) are shown in Fig. 6a at selected temperatures between 80 and 360 K. Since the X-ray wavelength here is different from the synchrotron source, the Bragg peaks differ in positions compared to Fig. 2a. It is clearly seen that the data at 300 K and 360 K are similar, alluding to the same phase. A Le Bail fit shows excellent agreement with the $Im\bar{3}$ space group at both 300 K and 360 K as depicted in Fig. 6b. The similarity of the XRD data at 300 K and 360 K is consistent with the inflection point seen at 288 K in Fig. 5a, suggesting that the film is in the cubic II phase at room temperature. Between 162 and 288 K, when the sample is in the tetragonal phase, the resistance increases monotonically. A Le Bail fit of the 240 K PXRD data yields the tetragonal (SG: *I4/mcm*) phase (Fig. 6b). Below 160 K, the PXRD data fit the orthorhombic phase. Overall, the resistance versus temperature data agrees well with the structural phase transformations in the $MAPbI_3$ sample grown on SiO_2. However, there are several open questions: the inflection point at 56 K in the resistance data may reflect an unexplored structural or isostructural phase transformation. There are stark differences in the trends in resistance for the two films shown in Fig. 5. We have further measured the lateral resistance in a single-crystal $MAPbI_3$ (which is in the tetragonal phase under ambient conditions) under illumination as a function of temperature. The crystal exhibits similar behavior to the CVD-grown film on glass along with a slight increase in resistance from 50 to 160 K when the crystal is the orthorhombic phase.

Our results show a clear distinction in temperature-dependent transport properties for $MAPbI_3$ films that exist in the cubic phase under ambient conditions versus films that are in the tetragonal phase. The room-temperature resistivity of the ambient cubic sample is 12 Ωcm, a value several orders of magnitude below typical resistivities for $MAPbI_3$ thin films, suggesting that the specific phase may result in a self-doping process, which may arise from local-charged defects [30]. It is worth pointing out that the trend of increasing resistance with temperature in the tetragonal phase is similar to what is seen in doped $MASnI_3$ [27, 30]. Currently, only $MAPbI_3$ films grown on SiO_2 have demonstrated the room-temperature cubic phase. We are exploring changes in the growth parameters in our CVD method to discover what other conditions may result in the ambient cubic phase. It should be pointed out that other CVD methods have also allowed for $MAPbI_3$ films in the ambient cubic phase through the introduction of an additional growth step which introduces another precursor material [13].

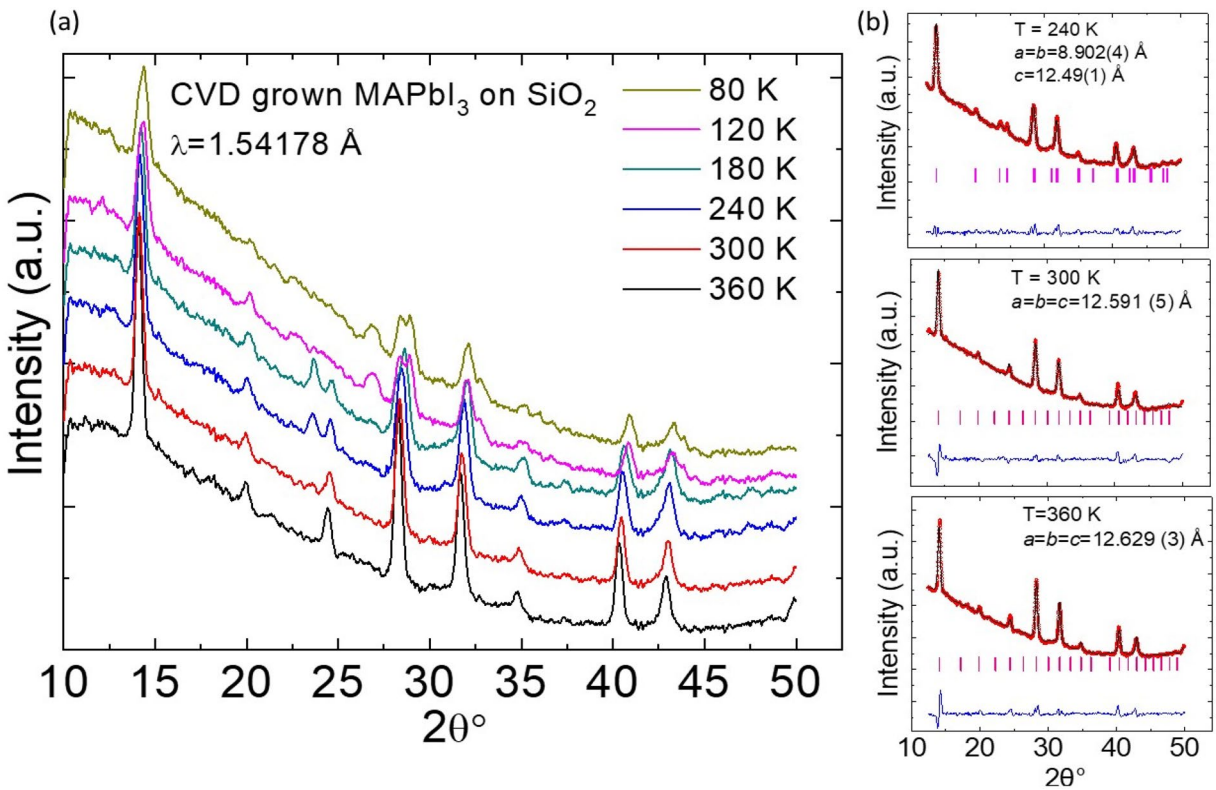

Figure 6: (a) PXRD pattern from the same $MAPbI_3$ sample shown in Fig. 4a at selected values of temperature. (b) Le Bail fits of the XRD data at 240 K, 300 K, and 360 K. The experimental data are shown as red circles and the calculated data as the black line. The small vertical lines (magenta) are Bragg positions, and the blue pattern is difference spectra (residuals).

Conclusions

In conclusion, a two-step CVD growth of $MAPbI_3$ is seen to produce films with both high air stability and high propensity of existing in the cubic phase. As a function of pressure, starting from the tetragonal phase under ambient conditions, the cubic phase II ($Im\bar{3}$) is seen to be induced at pressures as low as 0.25 GPa even if the specific film did not exhibit the ambient cubic phase. Although further work is needed to discover the precise parameters that lead to the ambient cubic phase, variations in structural properties are observed as a function of the substrate. Charge transport measurements, which are extremely sensitive to the structural phase transformations, reveal sharp anomalies at 288 K, 162 K, and 56 K in a $MAPbI_3$ film grown on SiO_2. Temperature-dependent PXRD measurements were performed, which were consistent with the anomalies in the transport measurements. This result suggests that an unexplored isostructural phase transition for films exhibiting the ambient cubic phase may exist at 56 K. The charge transport measurements conducted on the ambient cubic phase film exhibits profoundly lower resistance compared to typical films or crystals that are in the ambient tetragonal phase, suggesting a possible self-doping effect and accentuation of electronic transport as opposed to ionic transport. This work demonstrates the manifestation of an ambient cubic phase in $MAPbI_3$ film without introduction of additional deposition steps or precursor materials.

Experimental methods

Materials and thin film growth

All chemicals, lead (II) iodide powder (99.5%) and methyl ammonium iodide (MAI) (Dyesol) salt, were purchased from Sigma Aldrich Inc. A three-zone tube furnace from MTI Inc. with a quartz tube of length 1 m was used for the growth of the $MAPbI_3$ films. A schematic of the setup is shown in Fig. 1. The CVD growth parameters were similar to our prior work [15]. Briefly, a base pressure of 10^{-2} mbar was maintained by an automated pressure regulating system. The deposition was carried out in two steps. First, a film of PbI_2 was grown; 200 mg of PbI_2 powder was placed in a ceramic crucible in the first zone and the substrates were placed approximately 10 inches away, downstream from the source. The source was set to 400 °C at a ramp rate of 10 °C/min. Both glass and SiO_2/Si substrates were used after organic and plasma cleaning. N_2 gas (300 mbar) at a flow rate of 100 sccm was introduced in the tube. The total deposition time was approximately 40 min. The films were allowed to cool to room temperature in the presence of the N_2 flow. A yellow PbI_2 film was formed on the substrates (Fig. 1 (step 1)).

The second step involves the conversion to perovskite, where approximately 300 mg of MAI powder was placed in a separate ceramic crucible in the first zone without disturbing the PbI_2 films in the second zone. The temperature of the crucible was ramped to 200 °C at a ramp rate of 10 °C/min. The MAI vapors were transported towards the PbI_2 thin films by a N_2 flow of 100 sccm, and the conversion was allowed for 90 min. A dark perovskite film was formed as seen in Fig. 1 (step 2). The final film thicknesses were between 350 and 450 nm.

Characterization

Laboratory XRD data were collected by a Bruker X8 Prospector diffractometer (Bruker AXS, Inc.; Madison, WI). The samples were irradiated using Cu-Kα radiation from a microfocus source (45 kV, 0.60 mA; $\lambda = 1.54178$ Å). The diffracted intensity was recorded on an Apex II CCD area detector held at a fixed 2θ value and a crystal-to-detector distance of 80 mm. A Cryostream 700 cryostat (Oxford Cryosystems, Oxford, UK) was used to control the sample temperature. Absorption measurements were carried using a Shimadzu UV–Vis spectrophotometer. Four-probe resistance measurements on the sample were performed in a cryogen-free 9 T magnet with a base temperature of ~ 5 K, using a high-quality resistivity bridge from Linear Research. The sample was slowly cooled at the rate of 0.5 K per minute during the electrical resistance measurement as a function of temperature.

High-pressure synchrotron XRD

The high-pressure XRD measurements were conducted at sector 13-BMD, GSECARS, at the Advanced Photon Source (APS) in Argonne National Laboratory using a micro-focused monochromatic X-ray beam of wavelength 0.3344 Å. A symmetric diamond anvil cell (DAC) was used to generate pressure. The culet size of the diamonds was 500 μm, and a stainless-steel gasket pre-indented with a hole of diameter of about 180 μm was the pressure chamber. Ne gas was used as a pressure-transmitting medium and was loaded at GSECARS in sector 13 of the APS. The pressure was determined using the standard ruby fluorescence technique [31]. The lattice parameters were extracted using the Le Bail method. The peak shape was modeled using a pseudo-Voigt function, and the profile parameters, R_B, R_P, R_{wp}, and χ^2 served as quantitative measures for the goodness of fit.

Acknowledgments

We acknowledge the support of this work through the U.S. National Science Foundation (NSF) under Grant No. DMR-1807263. DKS acknowledges the support by US Department of Energy, Office of Science, Office of Basic Energy Sciences under the grant no. DE-SC0014461. CJA was supported by the South African National Research Foundation (Grant No. 103621, 92520, and 93212) and the University of Missouri-University of Western Cape Linkage Program. Portions of this

work were performed at GeoSoilEnviroCARS (The University of Chicago, Sector 13), Advanced Photon Source (APS), Argonne National Laboratory. GeoSoilEnviroCARS is supported by the NSF– Earth Sciences (EAR – 1634415) and Department of Energy- GeoSciences (DE-FG02-94ER14466). Use of the COMPRES-GSECARS gas loading system was supported by COMPRES under NSF Cooperative Agreement EAR -1606856 and by GSECARS through NSF grant EAR-1634415 and DOE grant DE-FG02-94ER14466. This research used resources of the APS, a U.S. Department of Energy (DOE) Office of Science User Facility operated for the DOE Office of Science by Argonne National Laboratory under Contract No. DE-AC02-06CH11357. We thank Dr. Sorb Yesudhas for valuable discussions and fitting of the ambient room-temperature XRD data, Dr. Steven Kelley for the low-temperature laboratory-based XRD measurements, and Dr. Sergey Tkachev, GSECARS, APS for Ne gas loading in the DAC.

Author contributions

The manuscript was written through contributions of all authors. All authors have given approval to the final version of the manuscript.

Data availability

The data will be made available upon reasonable request.

Declarations

Conflict of interest On behalf of all authors, the corresponding author states that there is no conflict of interest.

References

1. A.K. Jena, A. Kulkarni, T. Miyasaka, Chem. Rev. **119**, 3036 (2019)
2. D. Weber, Z. Naturforsch B **33**, 1443 (1978)
3. H. Cho, Y.-H. Kim, C. Wolf, H.-D. Lee, T.-W. Lee, Adv. Mater. **30**, 1704587 (2018)
4. S. Yesudhas, R. Burns, B. Lavina, S.N. Tkachev, J. Sun, C.A. Ullrich, S. Guha, Phys. Rev. Mater. **4**, 105403 (2020)
5. F. Capitani et al., J. Phys. Chem. C **121**, 28125 (2017)
6. S. Bai et al., Nature **571**, 245 (2019)
7. J.E. Bishop, J.A. Smith, D.G. Lidzey, A.C.S. Appl, Mater. Interfaces **12**, 48237 (2020)
8. C.-W. Chen, H.-W. Kang, S.-Y. Hsiao, P.-F. Yang, K.-M. Chiang, H.-W. Lin, Adv. Mater. **26**, 6647 (2014)
9. R. Sheng, A. Ho-Baillie, S. Huang, S. Chen, X. Wen, X. Hao, M.A. Green, J. Phys. Chem. C **119**, 3545 (2015)
10. P. Luo, Z. Liu, W. Xia, C. Yuan, J. Cheng, Y. Lu, ACS Appl. Mater. Interfaces. **7**, 2708 (2015)
11. M.M. Tavakoli, L. Gu, Y. Gao, C. Reckmeier, J. He, A.L. Rogach, Y. Yao, Z. Fan, Sci. Rep. **5**, 14083 (2015)
12. M.R. Leyden, Y. Jiang, Y. Qi, J. Mater. Chem. A **4**, 13125 (2016)
13. J. Qiu, L.L. McDowell, Z. Shi, Cryst. Growth Des. **19**, 2001 (2019)
14. M.T. Hoerantner et al., ACS Appl. Mater. Interfaces. **11**, 32928 (2019)
15. S. Ngqoloda, C.J. Arendse, T.F. Muller, P.F. Miceli, S. Guha, L. Mostert, C.J. Oliphant, A.C.S. Appl, Energy Mater. **3**, 2350 (2020)
16. T. Baikie, Y. Fang, J.M. Kadro, M. Schreyer, F. Wei, S.G. Mhaisalkar, M. Graetzel, T.J. White, J. Mater. Chem. A **1**, 5628 (2013)
17. F. Brivio et al., Phys. Rev. B **92**, 144308 (2015)
18. M. Szafrański, A. Katrusiak, J. Phys. Chem. Lett. **7**, 3458 (2016)
19. A. Jaffe, Y. Lin, C.M. Beavers, J. Voss, W.L. Mao, H.I. Karunadasa, ACS Cent. Sci. **2**, 201 (2016)
20. R.J. Elliott, Phys. Rev. **108**, 1384 (1957)
21. H. Haug, S.W.A Koch, Quantum Theory of the Optical and Electronic Properties of Semiconductors, Quantum Theory of the Optical and Electronic Properties of Semiconductors
22. J.-H. Lee, A. Jaffe, Y. Lin, H.I. Karunadasa, J.B. Neaton, ACS Energy Lett. **5**, 2174 (2020)
23. P.S. Whitfield, N. Herron, W.E. Guise, K. Page, Y.Q. Cheng, I. Milas, M.K. Crawford, Sci. Rep. **6**, 35685 (2016)
24. A. Musiienko et al., Energy Environ. Sci. **12**, 1413 (2019)
25. G.Y. Kim, A. Senocrate, T.-Y. Yang, G. Gregori, M. Grätzel, J. Maier, Nat. Mater. **17**, 445 (2018)
26. M. Keshavarz et al., Adv. Mater. **31**, 1900521 (2019)
27. C.C. Stoumpos, C.D. Malliakas, M.G. Kanatzidis, Inorg. Chem. **52**, 9019 (2013)
28. V. Campanari, M. Lucci, L.A. Castriotta, B. Paci, A. Generosi, M. Guaragno, R. Francini, M. Cirillo, A.D. Carlo, Appl. Phys. Lett. **117**, 261901 (2020)
29. F. Palazon, D. Pérez-del-Rey, B. Dänekamp, C. Dreessen, M. Sessolo, P.P. Boix, H.J. Bolink, Adv. Mater. **31**, 1902692 (2019)
30. C.C. Stoumpos, M.G. Kanatzidis, Acc. Chem. Res. **48**, 2791 (2015)
31. M. Knaapila, S. Guha, Rep. Prog. Phys. **79**, (2016)